Additive Manufacturing 96 (2024) 104539

Contents lists available at ScienceDirect

Additive Manufacturing

journal homepage: www.elsevier.com/locate/addma

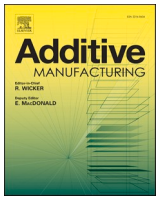

Non-destructive evaluation of additively manufactured superalloy IN718 via integrating microfocus X-ray computed tomography and non-linear acoustics

I-Ting Ho [a,b,*], Krishna Muralidharan [a,b], Sammy Tin [b], Devin Bayly [c], Brian Gockel [f], Michael Reale [f], Tribikram Kundu [a,b,d,e]

[a] New Frontiers of Sound Science and Technology Center, University of Arizona, Tucson, AZ, 85721, USA
[b] Department of Materials Science and Engineering, University of Arizona, Tucson, AZ 85721, USA
[c] Department of Research & Discovery Tech, University of Arizona, Tucson, AZ 85721, USA
[d] Department of Civil and Architectural Engineering and Mechanics, University of Arizona, Tucson, AZ 85721, USA
[e] Department of Aerospace and Mechanical Engineering, University of Arizona, Tucson, AZ, 85721, USA
[f] Lockheed Martin Corporation, USA

ARTICLE INFO

Keywords:
Sideband peak counting
Non-destructive evaluation
Micro-XCT
Porosity
Laser powder bed fusion

ABSTRACT

Superalloy IN718 components manufactured by laser powder bed fusion (PBF-LB/M) were non-destructively evaluated by the sideband peak counting (SPC) nonlinear acoustics method and suitably validated by microfocus X-ray computed tomography (XCT). A wide-band chirp acoustic wave was used to inspect the microstructures of IN718 samples with five distinct process parameters, and the results reveal that the number of sidebands, which result from the non-linearity induced by porosity, is significantly influenced by the distribution and size of pores, in addition to the volume fraction. There was a clear correlation between extent of porosity and the corresponding value of the SPC index. XCT analysis corroborated these findings, providing quantitative insights into the porosity characteristics that affect the ensuing acoustic responses. The findings demonstrated that the porosity with varying sizes and distributions generate different SPC profiles, which were correlated to XCT results to quantitatively assess the size and spatial distributions of the porosity. Fusion of SPC and XCT characterization techniques provides a new strategic approach for non-destructive testing, where the SPC method offers rapid, qualitative evaluation, while XCT provides detailed spatial resolution for defect quantification. The integration of SPC could lead to the development of more cost-effective and advanced quality control protocols, ensuring the reliability of AM-manufactured components regardless of their geometry and composition.

1. Introduction

Additive manufacturing (AM) encompasses a range of technologies where materials are consolidated in layers to construct complex 3D components. For fabrication of superalloy components, laser powder bed fusion (PBF-LB/M) further stands out among fusion-based AM techniques. It is suitable for producing structural parts intended for use in high performance applications, including aerospace, medical, and motor racing applications. Essentially, PBF-LB/M uses a laser to fuse specific sections of powder in a thin material layer with a predefined scan strategy based on the computer-aided design (CAD) model geometry to achieve the desired features. The same process is repeated for the subsequent layers until a 3D part is fabricated. In recent years, numerous studies have shown that PBF-LB/M can be used to fabricate high strength superalloys such as IN718 [1–3], IN738LC [4], CM247LC [5], C263 [6], and Hastelloy X [7] for marine and aerospace applications.

The ability of PBF-LB/M to successfully fabricate fully dense and crack free superalloy components, however, can be closely linked to their intrinsic weldability and chemistry. Generally, extreme temperature gradients encountered in all high energy density processes can induce issues like hot tearing and cracking during solidification of non-weldable Ni-base superalloys [8–15]. The high energy density accompanied with fast laser scanning speeds can also lead to the formation of keyhole porosity due to the vaporization of the material and the surface tension [16,17]. While cracks and keyhole porosity are formed due to the high energy input, lack-of-fusion (LoF) induced porosity are formed

* Corresponding authors.
E-mail address: iho@arizona.edu (I.-T. Ho).

https://doi.org/10.1016/j.addma.2024.104539
Received 30 June 2024; Received in revised form 4 November 2024; Accepted 4 November 2024
Available online 14 November 2024

Table 1
Scan parameters used for the PBF-LB/M process. Note that the nominal IN718 scan parameters, including a laser power of 1000 W, a scanning velocity of 2100 mm/s, a laser spot size of 275 μm, a hatch spacing of 0.14 mm, and a layer thickness of 50 μm, were optimized for the Velo3D Sapphire printer.

	Scan parameters compared with nominal parameters
Sample 1	30 % spot size reduction
Sample 2	20 % Power reduction
Sample 3	Same as nominal parameters
Sample 4	20 % Power reduction
Sample 5	Same as nominal parameters

as a result of the low energy density of the laser and usually has an irregular shape [17,18].

Since the presence of pore-like defects in structural materials is undesirable as they act as stress concentrations, defect characterization becomes a crucial technique for evaluation of the quality of PBF-LB/M parts. Generally, detection of defects is destructive and requires conventional metallographic procedures, including cutting, mounting, grinding, polishing, and etching before observation under a microscope. However, this method confines the analysis into a specific cross-section, and hence many features may be missing if the defects are non-uniformly distributed. Therefore, non-destructive testing (NDT) techniques are usually applied to provide an overview of internal structures including porosities and cracks to establish a quick evaluation of processing parameters. As a quantitative measurement method, microfocus X-ray computed tomography (XCT) has been used successfully to measure the physical density of objects and estimate the distribution, sizes, and shapes of micron-sized defects, using a calibration set based on the magnitude of attenuation coefficient [19]. Recently, a variety of studies have involved XCT to evaluate potential crack initiation sites [20–22] or to combine with in-situ monitoring for tracking the formation of various types of defects for the AM processed Ni-base superalloys [23–25].

While microfocus XCT is a powerful tool, it has some intrinsic limitations. For high atomic number materials, the ability to resolve small defects ($< 100\,\mu m$), such as cracks, cavities, and porosity, requires extended scanning times over a smaller detection area, especially when higher spatial resolutions are needed. In search of alternatives, ultrasonic techniques (UT) have been explored extensively. When a wave propagates through a non-linear media (e.g. metal parts with porosity), unlike the linear responses such as reduction in amplitude due to attenuation and scattering of the material [26], material interactions between these waves of different frequency at the interfaces of defects produce non-linear waves due to frequency modulation or higher harmonic effects. To characterize this variation, three common UT techniques were proposed:

The Higher Harmonic Generation (HHG) Technique operates on the principle of detecting nonlinearity in a range of materials via a quadratic nonlinearity parameter [27]. It is particularly sensitive to defects induced by material fatigue [28,29]. Since second harmonic components can also be generated as a result of the instrumentation nonlinearities, such as amplifiers, transducers, and coupling media, discerning between different sources of nonlinearities becomes the biggest challenge. Utilizing two-wave or three-wave mixing techniques [30] along with the selection of lamb waves should mitigate some of these issues, but this also increases the difficulties for experimental setups [31].

Nonlinear Wave Modulation Spectroscopy (NWMS) or Frequency Modulation Technique works by exciting two distinct waves in a specimen: a pumping wave with high amplitude but low frequency to induce stresses within the samples, and a probing signal characterized by its low amplitude but high frequency to sense the variation of modulus produced by the pump vibration [32]. This vibro-acoustic modulation technique was commonly used to detect localized defects such as cracks in structural parts [33,34]. Since only specific excitation frequencies satisfy the conditions required for generating sidebands, the selection of the probing and pumping frequencies for NWMS experiments still remains challenging for detecting defects and porosity in an unknown material.

The Nonlinear Impact Resonance Acoustic Spectroscopy (NIRAS) functions by monitoring frequency variations correlated with the excitation amplitude. Typically, a specimen is struck with an impactor, which induces it to a downward resonance peak shift as the strain amplitude increases. This technique is widely employed for detecting micro-cracks within composite materials [35,36]. However, it does have a limitation on the size of specimens and falls short when large defects need to be identified.

Among these methodologies, the Sideband Peak Counting (SPC) technique, which was first introduced in Kundu et al. [37], offers distinct advantages. Instead of measuring the amplitude of peaks induced by nonlinear interaction as waves propagate, the peaks of the sidebands above a threshold value are counted, and an increased number of weak spectral peaks appear when defects are present [37,38]. By averaging the number of peaks counted at thresholds from low to high, a single number of SPC index can be extracted to evaluate the degree of nonlinearity of a material [39]. Its mechanism revolves around the quick examination of defects without the necessity for precise guided wave mode generation as the incident wave. The inherent feature not only speeds up the analysis but also reduces preparatory steps and complexities tied to guided wave accuracies, and hence numerous studies have focused on the use of SPC technique to characterize the presence of internal defects such as cracks, delamination, and impact damage [40–46].

However, as promising as SPC seems, none of the existing studies have quantitatively resolved differences in the spatial distribution, size, and volume fraction of defects using the SPC method. Therefore, this study compares SPC and XCT results of five distinct IN718 samples processed by PBF-LB/M that have been engineered with varying porosity attributes. By integrating the qualitative information from SPC with the quantitative evaluations from XCT, this research aims to develop more effective approaches for evaluating the porosity structures in AM materials through ultrasonic defect analysis. The results from these samples were also be benchmarked against cross-sectional characterization using optical microscopy (OM) to ensure accuracy.

2. Theoretical background

2.1. Mathematical description of sideband generation

Assuming a nonlinear material be excited by elastic waves of two different frequencies, f_1 and f_2 (or angular frequencies ω_1 and ω_2), the total displacement field induced by elastic waves can be expressed by the following equation [38]:

$$u(x,t) = A_1(x)\sin(\omega_1 t) + B_1(x)\cos(\omega_1 t) + A_2(x)\sin(\omega_2 t) + B_2(x)\cos(\omega_2 t) \quad (1)$$

where A_1 and A_2 are the amplitudes of the sine components, while B_1 and B_2 are the amplitudes of the cosine components of the displacement field in terms of the oscillatory motion, representing the magnitude and phase of the elastic waves at frequencies f_1 and f_2. For one-dimensional wave movement, the strain field created within the material can further be derived as [38]:

$$\varepsilon(x,t) = \frac{\partial u(x,t)}{\partial x} = A_1'(x)\sin(\omega_1 t) + B_1'(x)\sin(\omega_1 t) \quad + A_2'(x)\sin(\omega_2 t) + B_2'(x)\cos(\omega_2 t) \tag{2}$$

Considering the classical nonlinear quadratic stress-strain relation, the total stress field associated with the strain field from equation is defined as [38]:

$$\sigma(x,t) = [E_0 + E_1(\varepsilon)]\varepsilon(x,t) = E_0\begin{bmatrix} A_1'(x)\sin(\omega_1 t) + B_1'(x)\sin(\omega_1 t) \\ +A_2'(x)\sin(\omega_2 t) + B_2'(x)\cos(\omega_2 t) \end{bmatrix} + E_1\begin{bmatrix} N_1(x)\sin(2\omega_1 t) + N_2\sin((2\omega_2 t)(\omega_1 t)) \\ +N_3(x)\sin((\omega_1+\omega_2)t) + N_4(x)\sin((\omega_1-\omega_2)t) \\ +N_5(x)\cos(2\omega_1 t) + N_6(x)\cos(2\omega_2 t)(\omega_1 t) \\ +N_7(x)\cos((\omega_1+\omega_2)t) + N_8(x)\cos((\omega_1-\omega_2)t) \end{bmatrix} \tag{3}$$

Here, the first-order nonlinear elastic modulus $E_1(\varepsilon)$ explicitly depends on the strain ε, capturing the primary nonlinear response of the material. The multiplying factors N_1, N_2,……, N_8 for different trigonometric terms are functions of A_1', B_1', A_2', B_2'. While it is possible to introduce higher-order nonlinear terms, i.e. $E_2(\varepsilon)$, $E_3(\varepsilon)$, etc., to capture more complex nonlinear behaviors, the first-order term typically has the most dominant effect on the nonlinear response. Higher-order terms often contribute significantly less to the overall behavior and can be considered negligible in many practical scenarios.

From Eq. 3, it could be seen the non-linear term with frequencies other than ω_1 and ω_2 generates waves with frequencies $2\omega_1$ and $2\omega_2$ (higher harmonic waves) as well as $\omega_1 \pm \omega_2$ (modulated waves), and more waves would be generated if higher order terms are included. These modulated waves are considered as sideband peaks or simply sidebands.

2.2. Sideband peak count technique

When a broadband pulse laser signal propagates through an inspection area with non-linearity induced by defects, nonlinear wave modulation can occur among various frequency components excited by the input signal. To identify these nonlinear modulations, the spectral density distribution $P_x(f)$ should be calculated from the time-signal function $x(t)$ using the following correlation [38,41,43]:

$$P_x(f) = E[X(f)X'(f)] \tag{4}$$

where $X(f)$ is the Fourier transform of $x(t)$ and the "prime" denotes the complex conjugate. $P_x(f)$ within selected frequency range is then normalized to fit its values within unity.

The SPC is defined as the ratio of the number of spectral peaks (N_P) above a threshold (T) to the total peak number (N_T) in $P_x(f)$ within the specified spectral frequency range. A lower limit (LL) is defined to avoid influence from noise, and SPC values are determined when T moves from LL to 1, i.e. upper limit, UL, using the following correlation:

$$SPC(T) = \frac{N_P(T)}{N_T} = \frac{N_P(T)}{N(LL) - N(UL)} \tag{5}$$

As the level of non-linearity increases, more sideband peaks show up in the spectrum or the sideband amplitude increases proportionally. Therefore, the SPC plot will show larger values as the number of defects increases.

3. Experimental procedure

3.1. Materials

Gas atomized IN718 powder with a chemical composition consistent with ASTM standard B637 was used in this investigation. The PBF-LB/M process was carried out by Lockheed Martin Corporation, USA using a Velo3D Sapphire printer to fabricate tensile bars in an inert Argon gas atmosphere using five customized process conditions. The core parameters are shown in Table 1. Customized scan patterns, generated by the embedded Flow 4.0 software, were implemented to create different sizes, fractions, and distributions of porosity in each sample. This approach facilitated a systematic evaluation of the SPC technique's capability to differentiate these engineered variations. These five distinct samples were part of a build that included 148 tensile bars, which were stacked and distributed in 74 build plate locations. All samples were built in near-net shape without subsequent machining. The dimension of tensile bars and the building direction during the PBF-LB/M process are illustrated in Fig. 1, and the area of interest for both ultrasonic test and X-ray computed tomography is highlighted by a red dotted box.

3.2. Ultrasonic inspection

The experimental configuration used for ultrasonic testing is depicted in Fig. 2(a). A computer controls a BK Precision 4055B function generator and a Tektronix MDO3024 oscilloscope. To allow the nonlinearity in the specimen to interact with whichever frequency it is sensitive to, a wide band chirp signal (0–400 kHz) was sent and propagated through the samples, generating the sidebands [37]. The signals were then amplified to a peak-to-peak voltage (Vpp) of 20 V through a PD200 amplifier, and an Olympus PZT transducer was linked to the amplifier and transform the electrical signal to the sound wave which propagated through the samples. Subsequently, the output waves were received by the other PZT transducer and the final signals were recorded by the oscilloscope that was connected to the computer.

In order to further compare the SPC results with XCT visualization in a selected area, transducers were clamped with samples by a fixture to allow acoustic wave travel through the center of gauge section, as shown in Fig. 2(b). The analytical procedures were displayed in Fig. 3. The time signal data was collected and were used to estimate the number of sidebands for further analysis, as illustrated in Fig. 3(a). The receiving signals under time domain were then calculated using a Fast-Fourier Transform (FFT) method in Matlab to obtain the side bands under the frequency domain (Fig. 3(b)). The amplitude was normalized to standardize the thresholding procedure and fix the upper limit of threshold to be 1. The SPC value was subsequently determined by counting the peaks above the selected threshold and below the upper limit. To minimize the test noise induced by environmental and operational conditions which can deteriorate the performance of the SPC technique, the lower limit was set to be 0.07 (see Fig. 3(c)).

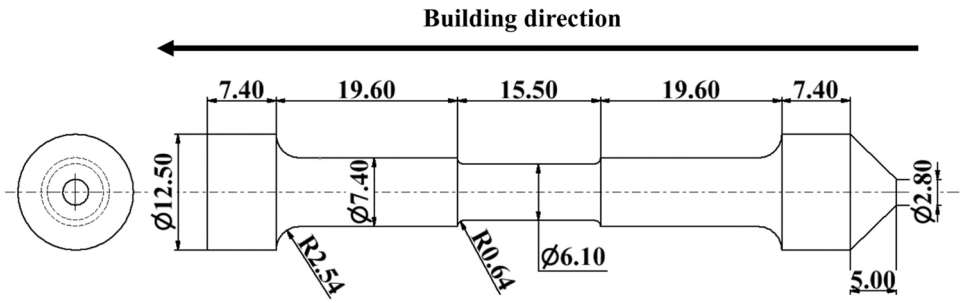

Fig. 1. Schematic illustration showing the sample dimensions of tensile bars. The area of interest for both ultrasonic test and X-ray computed tomography is highlighted by a red dotted box.

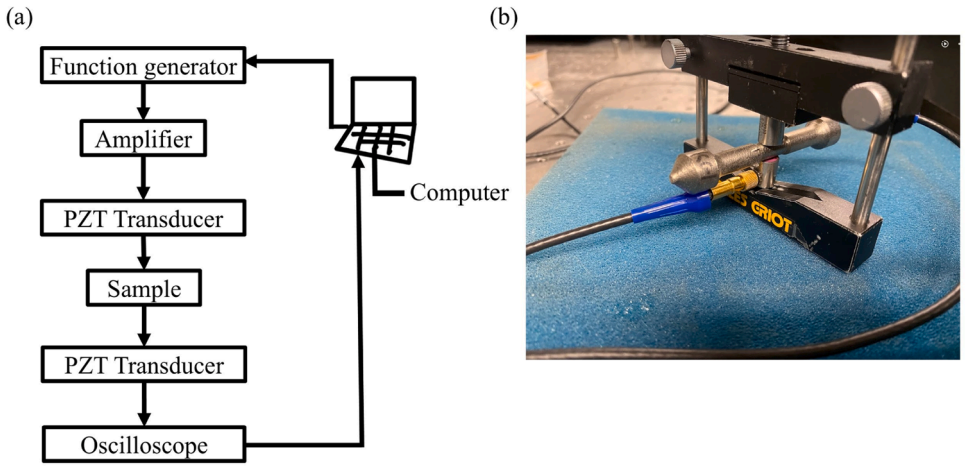

Fig. 2. (a) Experimental configuration for ultrasonic testing and (b) photo showing the fixture fixing the transducers to detect the acoustic response from the gauge section.

3.3. Microfocus X-ray computed tomography (XCT) set-up and experimental test parameters

The gauge section of five distinct specimens (see Fig. 1) were analyzed non-destructively for the shape and size of their internal structures using a Shimadzu InspeXio™ SMX™-225CT FPD HR Plus Microfocus X-ray computed tomography (XCT) with a detector pixel pitch of 139 μm. Settings used for the evaluation for all samples are displayed in Table 2, and a 2 mm thick copper plate was utilized to harden the spectrum. The resolution limit of this system was determined by the combination of tube current and tube voltage. Parameters used in the present study allow the system to resolve a line size of 7 μm, which is close to the selected voxel size. The small enough voxel size allowed for the quantitative analysis of voids with diameters larger than 10 μm. The projection data with an image resolution of 2048 × 2048 were then corrected for beam hardening and visualized using open-source software Paraview 5.11.0 [47]. For better standardization during the porosity structure analysis, the iso-value selected for binarization was fixed at 50 % within the range between the peaks contributed by the matrix and porosity, respectively, from the transfer function illustrated by a histogram (see the example in Fig. 4).

The selected pixels were processed using the "Tetrahedralize" and "Extract surface" algorithms embedded in Paraview to generate a volume mesh, which helped define the interface of each object in the next step. Surface approximation and extraction was then carried out using the algorithm 3D VESPA Alpha Wrapping from the Computational Geometry Algorithms Library (CGAL) to generate a valid triangulated surface mesh that strictly contains the inputs as determined by the binarized XCT data [48–50]. With the resulting valid surface meshes, object identification was carried out using the "Compute connected surface properties" filter in Paraview, which identifies objects with closed surfaces.

The results after binarization and surface extraction were validated by comparing the area fraction of porosities between the same image layers from the unprocessed XCT data and the results processed by binarization and VESPA Alpha Wrapping algorithm, respectively. As shown in Fig. 5, it could be seen that the images processed by binarization and surface extraction closely matched the unprocessed XCT images. Through the image analysis via default image thresholding algorithm using Image J software, whose results are shown in Table 3, the differences in area fraction of porosity are found to be below 0.5 % for all tested samples. The comparison demonstrates the reliability of binarization and surface extraction process to be used for correlating the acoustic results.

To visualize the volumetric properties of the porosities, an extended script was incorporated into the pipeline via the “Programmable filter” function to apply the volumetric data to each pore. The distribution of porosities was evaluated by estimating the center-to-center distances between one pore and its 20 nearest neighbors using the k-nearest neighbors method under the sklearn.neighbors library (Python) [51,52].

3.4. Validation by 2D defect characterization: digital microscopy

The gauge section of samples was sectioned in half via a Struers precision cut off wheel along the longitudinal direction for microstructural validation by OM. The sectioned samples were mounted using phenolic resin and prepared using standard metallographic procedures with a final grinding step with 1200 grit SiC paper followed by automatic polishing with 9 μm, 3 μm, and 1 μm diamond suspension as well as 0.05 μm alumina suspension. An area of 6 mm × 8 mm was captured

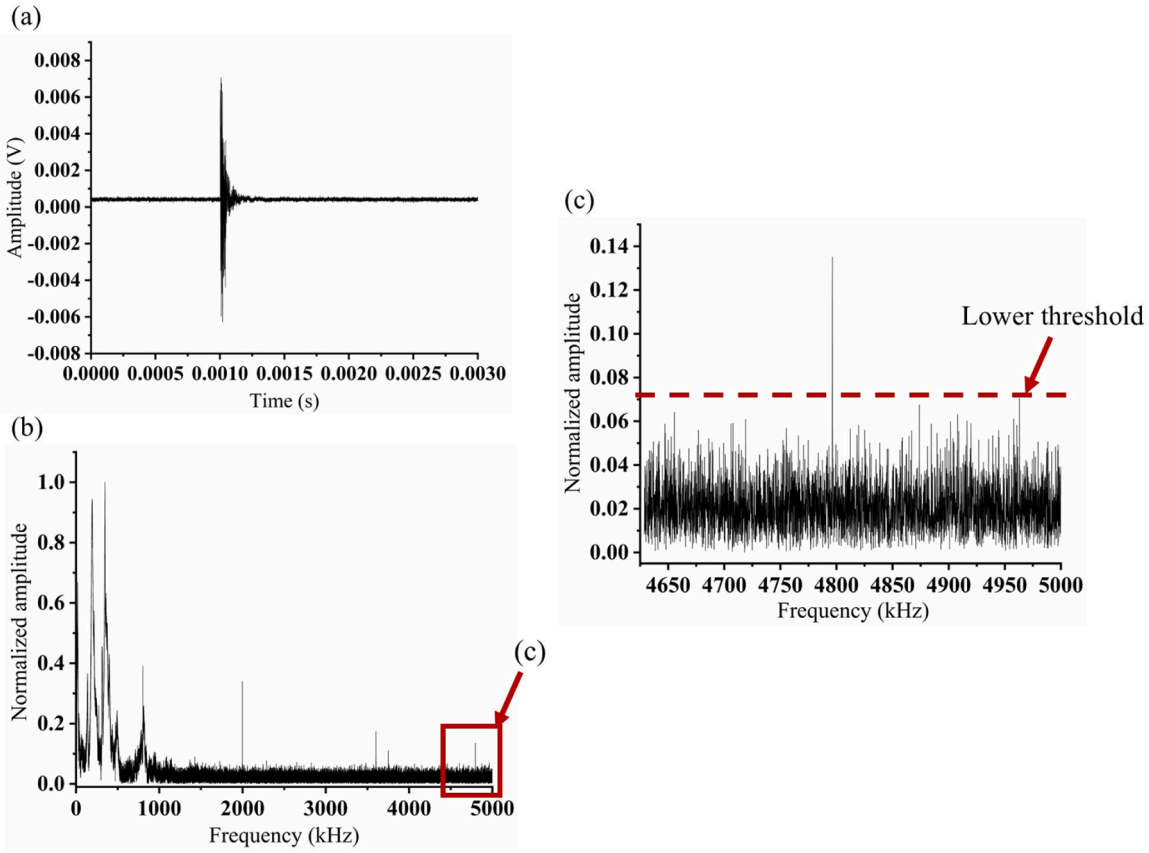

Fig. 3. (a) Transient response of sample 1; (b) FFT plot transformed from (a) with the lower threshold highlighted in (c).

Table 2
XCT parameters used in the present investigation.

Parameters	Value
Voltage (kV)	145
Current (μA)	100
Source to object distance (mm)	25
Source to image distance (mm)	800
Acquisition rate (fps)	4.5
Voxel size (μm)	6
Number of views	3600
Number of averages for each view	2

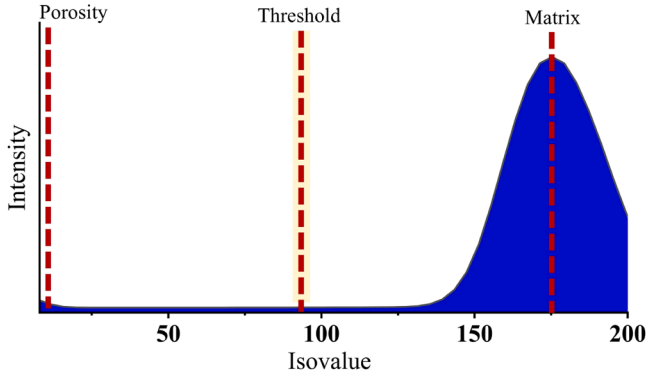

Fig. 4. Illustration showing the selection of binarization from the transfer function of XCT unprocessed data represented by a histogram. The example was taken from sample 1.

for each specimen with a pixel size of 2 μm using a Keyence VHX-7000 optical microscope; the subsequent measurements for pore size and area fraction were conducted using the Keyence image analysis software for comparison with the XCT observations.

4. Results

4.1. SPC analysis focusing on gauge area

Fig. 6(a) shows the FFT plots for the five distinct samples. It could be seen that samples 2 and 3 exhibit the most significant peaks at frequencies below 400 kHz. This trend was more pronounced in sample 2 as the peak at low frequency suppressed the relative intensity of peaks at higher frequencies after normalization. In contrast, samples 1, 4, and 5 show their peaks predominantly at higher frequencies, and the number of peaks with normalized intensity higher than 0.5 became larger leading to higher peak counts at higher thresholds, especially for sample 5. According to the plot showing the number of peak counts at different thresholds, Fig. 6(b), sample 5 exhibited more than 2500 peaks when the threshold value was set at 0.07. Moreover, unlike samples 2 and 3 whose number of peaks dropped rapidly before the threshold value increased to 0.5, the number of peaks for sample 5 only presented a slight drop before the threshold value reached 0.2 and decreased slowly until threshold value reached 0.7. Although less pronounced, samples 1 and 4 showed a similar trend to sample 5 leading to higher number of peaks in general when compared to samples 2 and 3. This observation is in agreement with the average SPC values which were greater for samples 1, 4, and 5 whereas less for samples 2 and 3, as shown in Table 4.

4.2. Visualization of porosity structure

To further quantify the level of defects and to evaluate the impact of

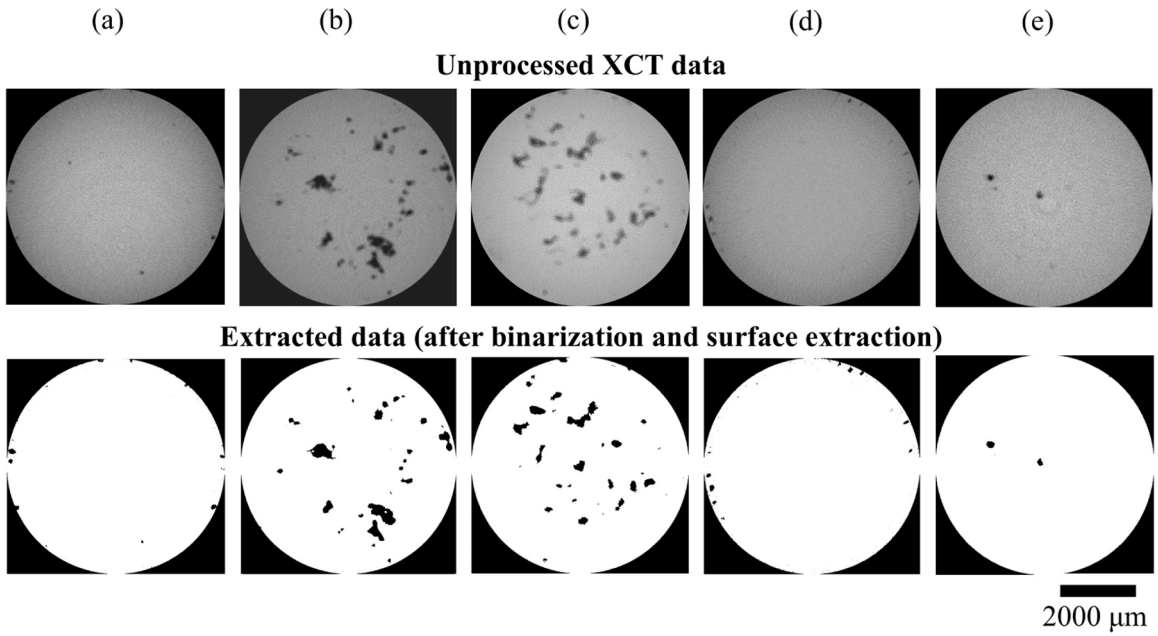

Fig. 5. Comparison of the same layers extracted from the unprocessed XCT data and extracted data via binarization and CGAL Alpha Vespa Wrapping algorithm, respectively, for (a) sample 1, (b) sample 2, (c) sample 3, (d) samples 4, and (e) sample 5.

Table 3
Summary of area fraction of porosity estimated from Fig. 5. The area fraction was evaluated by the ImageJ software and the binarization was carried out by the Default algorithm.

	Sample 1	Sample 2	Sample 3	Sample 4	Sample 5
Unprocessed XCT data					
Area fraction of porosity (%)	0.186	3.751	4.206	0.285	0.171
Extracted data (after binarization and surface extraction)					
Area fraction of porosity (%)	0.189	3.227	3.768	0.276	0.197

defects on the magnitude of SPC in different samples. Microfocus XCT analysis was carried out to reveal the morphologies and distribution of porosities within the gauge section of 5 distinct samples, as shown in Fig. 7. It could be seen that samples 2 and 3 possessed a high fraction of large, irregular porosity, accompanied by large number of finer porosities with more spherical morphology. On the other hand, samples 1, 4, and 5 contained mostly spherical porosity that was distributed differently within the gauge section. Through the statistical analysis for porosity within each sample, Fig. 8, the volume fraction, mean size, and maximum size of the porosity can be estimated, as shown in Table 5. It is noteworthy that samples containing the relatively higher volume fraction and pore size, such as samples 2 and 3, exhibited a smaller average peak count and magnitude of the SPC value. Furthermore, despite the same nominal volume fraction of pores, samples 1, 4, and 5 still presented large variations in number of peaks and SPC values from 625.6 and 0.26 to 371.7 and 0.19, respectively, which correspond to the decreasing mean size and maximum size of the porosity from 200 μm and 47.5 μm to 140 μm and 40.7 μm, respectively. These findings clearly suggest that the non-linear acoustic response is likely influenced by not only the number of defects, but also their size and distribution.

To better analyze the morphologies of non-spherical defects, the sphericity of porosities within each sample was estimated using the following equation [53]:

$$\psi = \frac{\pi^{1/3}(6V)^{2/3}}{A} \tag{6}$$

where V is defect volume and A is defect surface area. The objects are considered to be the perfect spheres when $\psi = 1$, and defects with $\psi < 0.5$ can be regarded as lack-of-fusion defects [54].

Fig. 9 displays the distribution of sphericity for porosities distributed within distinct samples; the porosities with the size below and beyond the mean size were analyzed separately to highlight the morphologies of large defects, as shown in Fig. 9(a) and (b), respectively. It could be seen that over 50 % of the porosity with the size smaller than the mean diameter showed the sphericities larger than 0.8 for samples 1, 4, and 5. Even though some porosity with the size beyond the mean diameter possessed sphericities smaller than 0.5, the relative frequencies of these irregular porosities was found to be below 30 % for samples 1, 4, and 5. This statistical finding indicates that there is a predominance of small, spherically shaped porosity in these samples as observed in the 3D visualization results, Fig. 7 and Fig. 8.

In contrast, 56 % and 78 % of porosity larger than the mean size were observed in sample 2 and sample 3, respectively. Despite the relatively lower fraction of the non-spherical defects, more than 50 % of fine porosity had a sphericity below 0.7. The analysis of sphericities has clearly suggested the morphologies of porosity in sample 2 and sample 3 are dominated by the elongated-shaped or irregularly-shaped defects.

Fig. 10 (a) shows the OM images revealing the cross-section of gauge area for five distinct samples. The statistical analysis shows that the equivalent volume fraction was estimated to be 0.047 %, 0.61 %, 0.18 %, 0.066 %, and 0.066 % for sample 1 to sample 5, respectively. These estimated volume fractions were similar to those evaluated from the XCT visualization results. The conditions and scan parameters used for the microfocus XCT analysis provide enough accuracy and spatial resolution to elucidate the variations in SPC results. In addition, the irregular or elongated porosity with sizes larger than 100 μm is consistent with the presence of lack-of-fusion defects ($\psi < 0.5$) within samples 2 and 3 as observed in the XCT results, Fig. 8 to Fig. 9. Similar observations showing the characteristic morphologies of lack-of-fusion defects revealed by XCT and metallographic characterization have been widely reported in the previous studies [55–57]. It should be noted, however, that there appeared to be differences in the pore size distribution between the samples 4 and 5. Comparison of the OM and XCT results, Fig. 10 (b), revealed a slightly larger size distribution of pores within the sample 4, when compared to the maximum and mean size of

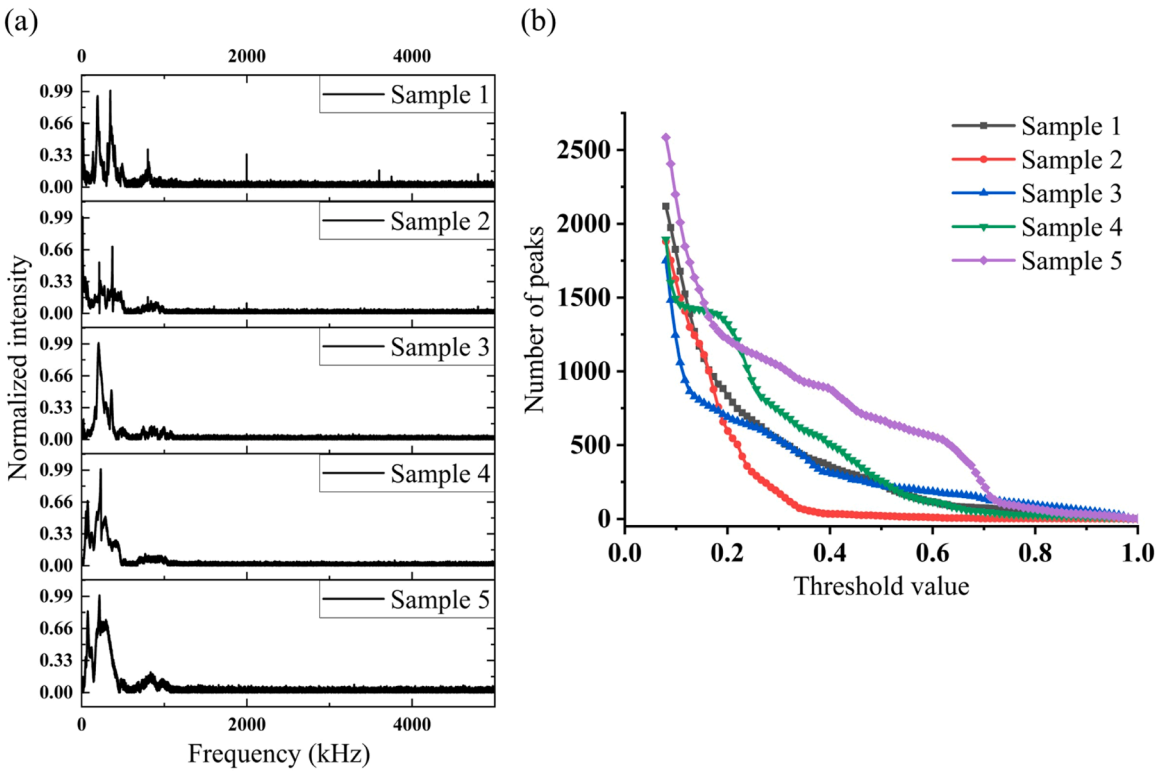

Fig. 6. (a) FFT plots and (b) SPC curves for the five samples.

Table 4
Summary of average number peak counts and SPC values for the five distinct samples.

	Sample 1	Sample 2	Sample 3	Sample 4	Sample 5
Average number of peaks	371.7	217.8	333.3	442.2	625.6
Average SPC	0.19	0.12	0.17	0.22	0.26

porosities estimated by XCT results. This variation might be attributed to the non-uniform distribution and irregular shapes of porosity within the samples 4 and 5 that are not captured in the 2D OM images.

5. Discussion

This investigation demonstrates that there are systematic variations in sideband peak generation that are induced by different volume fractions and sizes of pores in PBF-LB/M processed IN718. Comparison of the XCT, OM, and SPC results for the same samples has yielded illuminating insights into the relationship between pore structure and resulting acoustic response. Several key observations can be derived from our analysis.

5.1. *Influence of porosity structure on SPC response*

The SPC results from Fig. 6 and Table 4 have clearly demonstrated that sample 2 and sample 3 possessed less generation of sidebands leading to a rapid drop in counting of peaks as magnitude of threshold increased. Statistical analysis of XCT results (Fig. 8, Fig. 9, and Table 5) revealed a prevalence of large, irregularly shaped lack-of-fusion defects in samples 2 and 3. It is also interesting to note that the number of SPC did not necessarily increase with increasing volume fraction, as evidenced by comparing the average peak counts and SPC values with sample 1, sample 4, and sample 5. Although the volume fraction only differed by at most 0.01 %, the average peak counts and SPC varied significantly between sample 1 and sample 5, ranging from 371.7 and 0.19 to 625.6 and 0.26, respectively. Hence, it could be deduced that the volume fraction of porosity should not be the only factor contributing to the variations in non-linear acoustic response.

To further understand the other factors that may influence the sideband generation, the size distributions of pores analyzed from the XCT results were summarized in Fig. 11 (a) and (b). The median of the pore sizes can be estimated to be 72 μm, 196.3 μm, 264.9 μm, 66.6 μm, 128 μm for samples 1–5, respectively. By comparing samples 1, 4, and 5, it could be further seen that the volume fraction of pores larger than 150 μm increased by 2.5 % and 15 % approximately in sample 4 and sample 5 resulting in larger mean size and maximum size of porosity as presented in Table 5. Since the generation of sidebands arises from the relative opening and closing of an interface (kissing bonds, cracks and/or crack tips, porosity, etc.), if the defect size is small enough to cause non-linear effects, then more sideband peaks appear as the contacting area of surface increases by increasing size of defects [42,58]. Therefore, the presence of relatively larger pores in samples 4 and 5 likely accounts for the increase in both the number and amplitude of sidebands, resulting in higher SPC values compared to sample 1.

It should be noted, however, that the number of sidebands does not always increase with increasing pore sizes or volume fraction of defects. As the pore sizes exceeded a certain threshold, the number of sidebands decreased significantly accompanied with reduce normalized amplitude in samples 2 and 3. It is known that the non-linear acoustic response is generated when contact occurs along an interface. Under the same frequencies used for the elastic wave, it would be expected that the small pores come in contact more frequently causing higher nonlinearity in the material as the elastic wave passes through the specimens [37,43,59]. It has been reported earlier that SPC index increases at a faster rate initially with the increase of defect size (cracks, porosity etc.) and then its rate of increase goes down and can even become negative for different structures - welded joints in steel pipes [60,61], composite plates [39], concrete [44,45,62], and also for additively manufactured

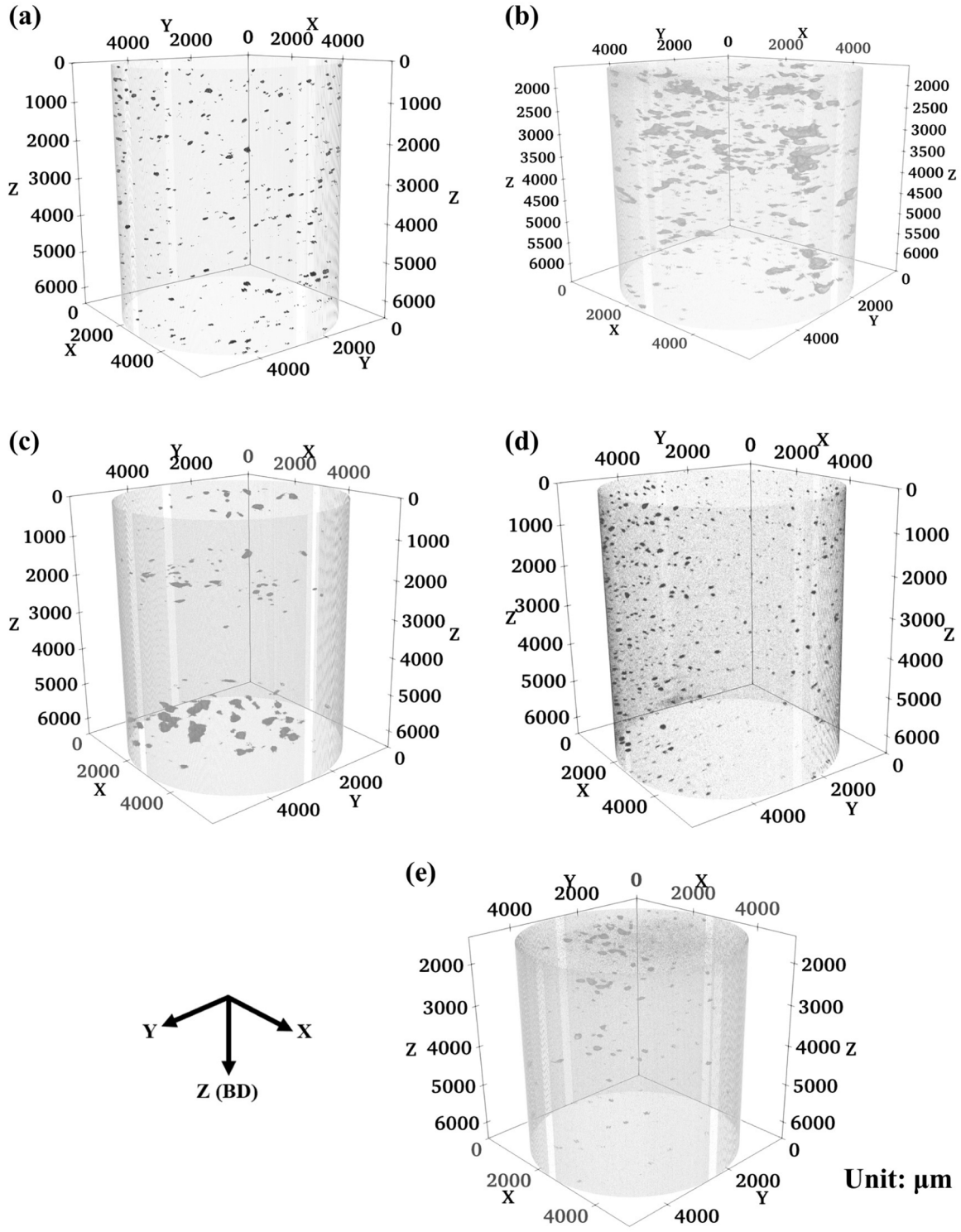

Fig. 7. XCT visualization results for (a) sample 1, (b) sample 2, (c) sample 3, (d) sample 4, (e) sample 5, respectively.

components [63]. Justifications of such observation have been provided through peri dynamics based peri-ultrasound modeling [59,64–66].

Even for larger pores, the effective surface area available for generating sidebands with sufficient amplitude would be limited to tips of these lack-of-fusion defects. The underlying mechanism is consistent with the lower measured SPC values in samples 2 and 3 as these large void spaces in the material's microstructure might not contribute as effectively to the nonlinear response as smaller, less connected voids in samples 1, 4, and 5.

Since it is known that the non-linear acoustic response, such as higher harmonics, are generated because of the structural inhomogeneity or elastic inhomogeneity regardless of whether the defects strengthen or weaken the matrix locally [58,67,68], the distribution of porosity might have also contributed to the variations in SPC results. To analyze the distribution of porosity, the center-to-center distances to neighbors of porosities were measured. By averaging the distances to the 20 nearest neighbors, the cumulative distribution of center-to-center distances for porosity in samples 1, 2, 3, 4, and 5 was determined and

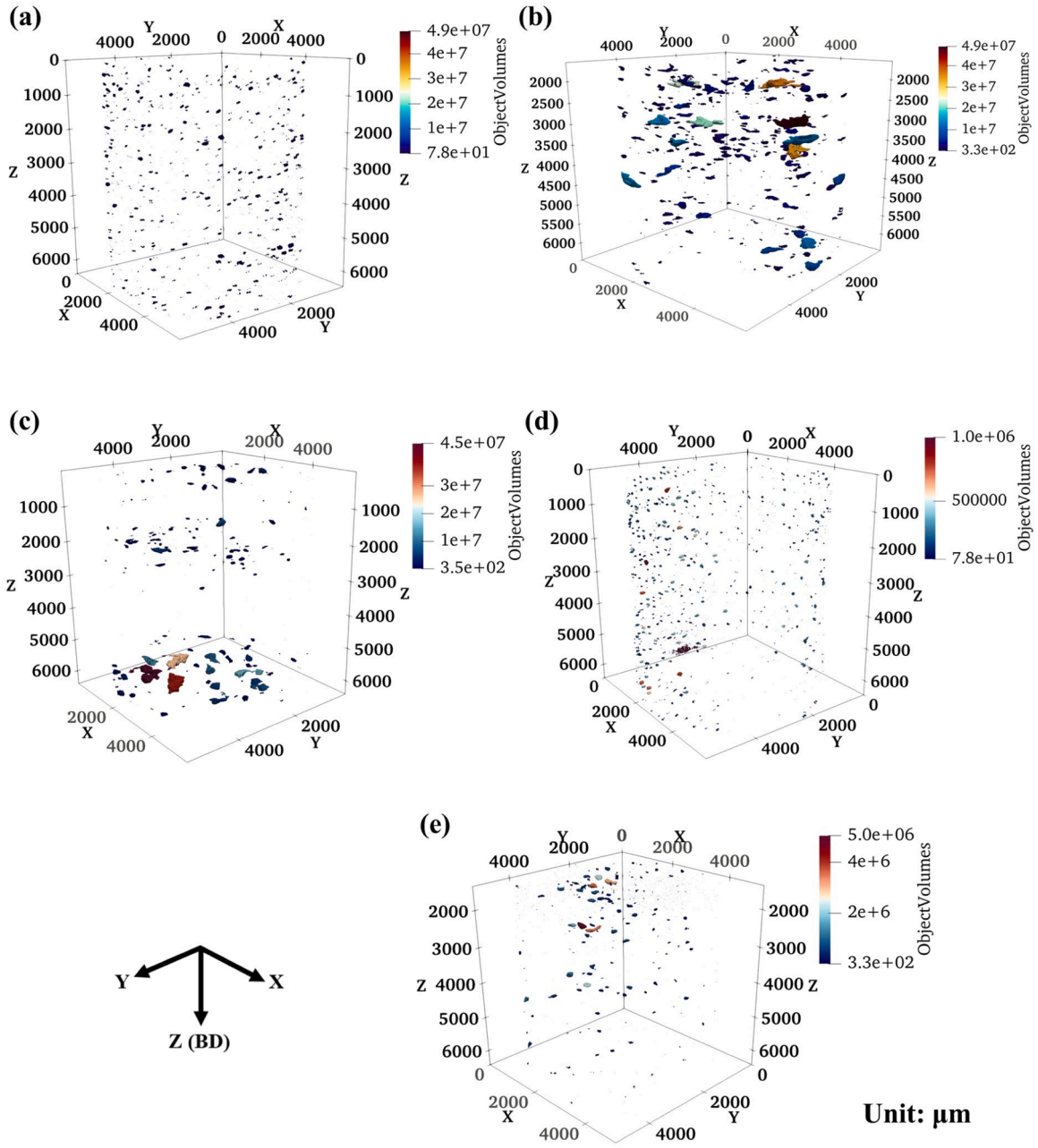

Fig. 8. Visualization of XCT results with binarization and surface extraction using CGAL algorithm for (a) sample 1, (b) sample 2, (c) sample 3, (d) sample 4, (e) sample 5, respectively. The porosities were colored differently based on their volume in μm^2.

Table 5
Summary of statistical analysis for size and volume fraction of pores across five distinct samples.

	Sample 1	Sample 2	Sample 3	Sample 4	Sample 5
Volume fraction (%)	0.03	0.66	0.17	0.04	0.03
Max/mean diameter (μm)	140/ 40.7	461/ 81.3	380/ 65.7	181/ 40.6	200/ 47.5

plotted in Fig. 12. Due to the significant increase in volume fraction from 0.03 % to 0.66 %, it could be expected that the porosity within sample 2 shared a shorter distance to their neighbors under the same volume of samples when compared with the other samples. It is interesting to note that despite the relatively higher volume fraction of 0.17 % and larger relative frequency of low-sphericity lack-of-fusion porosity, the extremely non-uniform distribution of large pores along specific layers (see Fig. 7 and Fig. 8) led to the increasing distance of pores to their neighbors. This may account for the relatively larger average SPC when compared with that of sample 2 as the sideband counts were averaged among the entire volume, which included those intact regions.

Despite containing a similar volume fraction of porosity, samples 1, 4, and 5 exhibited significantly different average distances between each pore. According to Fig. 12, the center-to-center distances to neighbors can be estimated to be 65 μm, 104 μm, 98 μm at the cumulative fraction of 50 % while 155 μm, 216 μm, and 259 μm at the cumulative fraction of 75 % for samples 1, 4, and 5, respectively. This observation is also supported by the XCT visualization corresponding to the reduced gauge volume that is cropped to contain only 90 % of the original diameter, Fig. 13. It is apparent that the number of pores decreased dramatically in sample 1, and the top view of visualization (Fig. 13 (c)) further indicates that there is a much higher tendency of porosity to be spatially

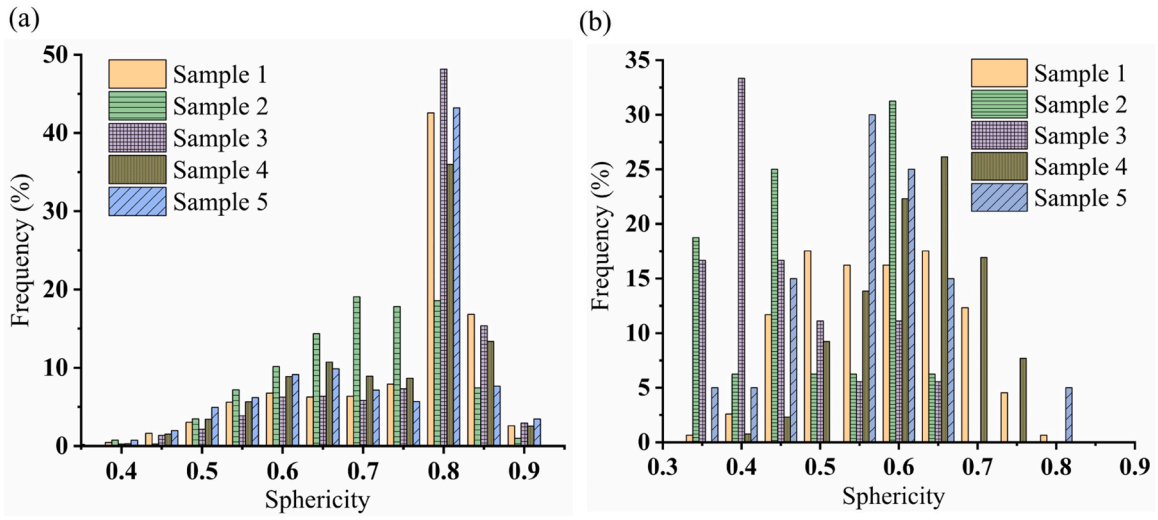

Fig. 9. Distribution of sphericity for porosity whose diameter (a) below the mean size of porosity and (b) beyond the mean size of porosity for 5 distinct samples.

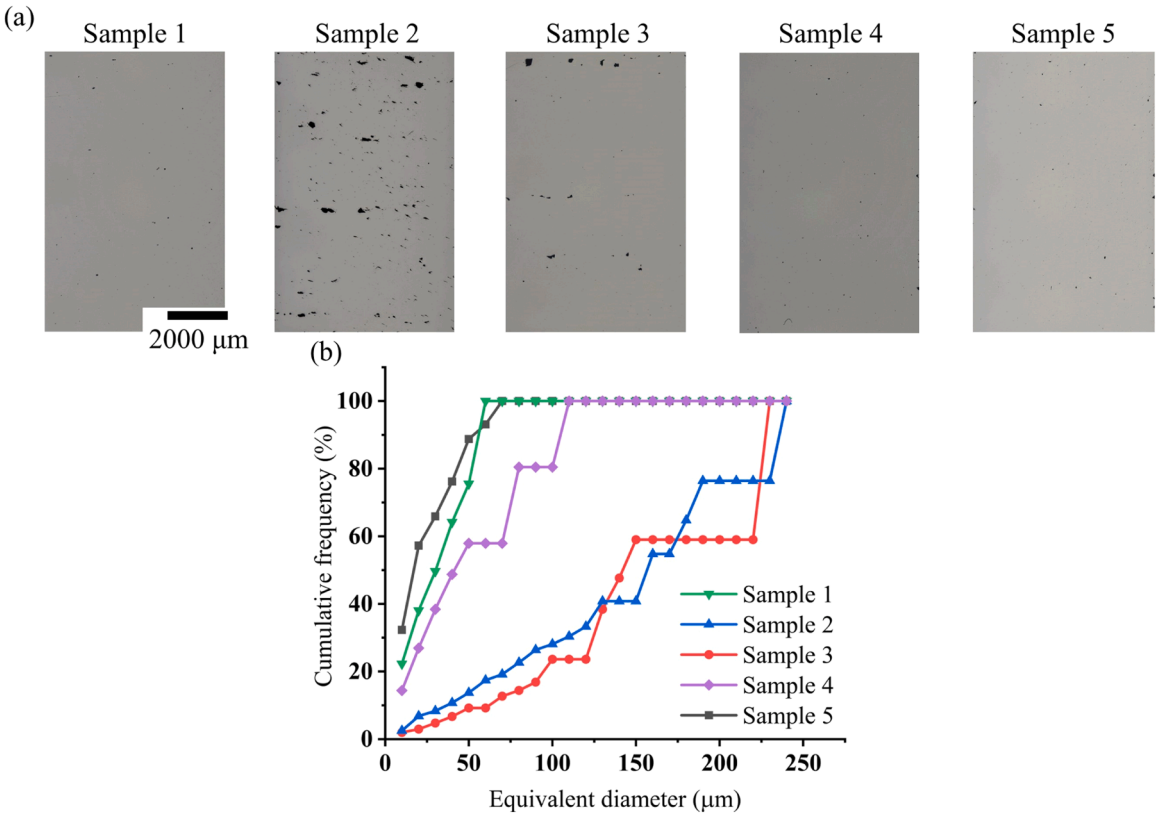

Fig. 10. (a) OM images showing the cross-sectional view of 5 distinct samples and (b) the corresponding volume-weighted pore size distribution for each sample.

distributed and concentrated near the samples' surface in sample 1, when compared to sample 5. Through the statistical analysis of the selected area, it is noteworthy that sample 1 exhibited a pronounced drop in volume fraction from 0.03 % to 0.0019 %, whereas sample 5 only exhibited a subtle decrease by 0.01 %. The findings strongly suggest that even for samples that contain similar volume fractions of porosity, sample 1 would be expected to have higher degree of clustering than that in samples 4 and 5. This variation is effectively captured in the SPC results where the value for sample 1 is 0.19, while relatively higher SPC values of 0.22 and 0.26 were determined for samples 4 and 5.

5.2. Comparison of methods for defects characterization

The comparative analysis of different defect detection methods—specifically ultrasonic testing via SPC, microfocus XCT, and metallographic characterization via OM—reveals complementary insights of the material's internal microstructure. Under proper conditions, the SPC method has shown the ability to accurately assess the overall integrity of materials without the constraints of sample size and resolution inherent to XCT. SPC is also unique in its ability to assess large material volumes quickly, making it an effective screening tool for preliminary qualitative analysis. Furthermore, unlike the dependence of XCT on the linear

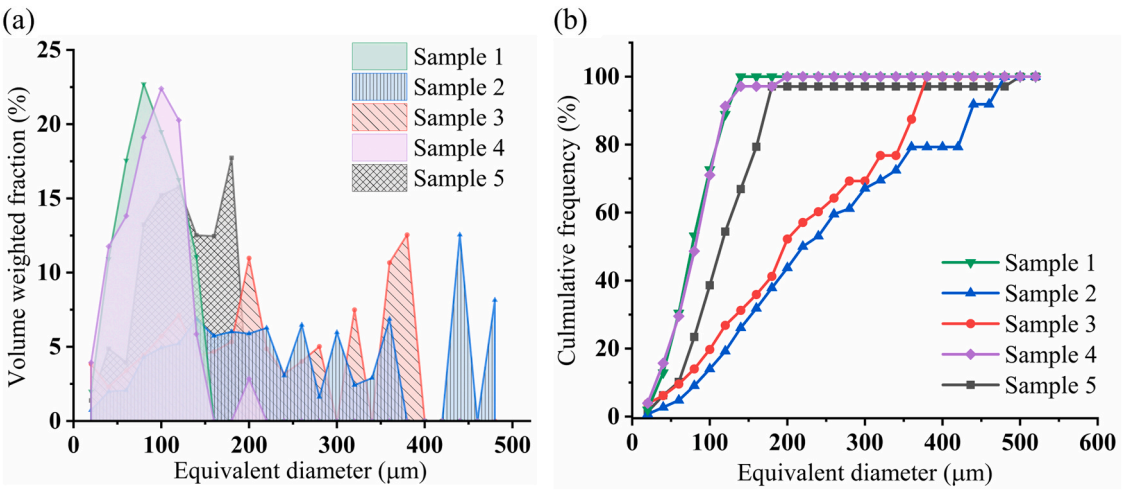

Fig. 11. Summary of pore size distribution in terms of (a) volume-weighted fraction and (b) cumulative volume-weighted fraction estimated by XCT data with binarization and surface extraction.

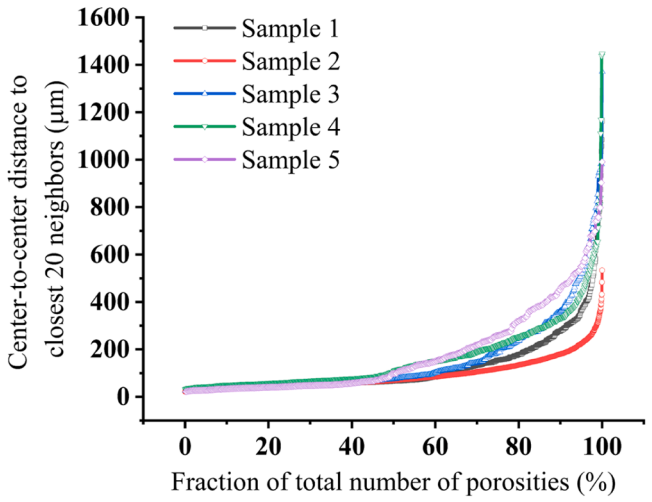

Fig. 12. Cumulative plots showing the fraction of porosity with different center-to-center distances between each pore and its nearest 20 neighbors.

attenuation of X-rays that limits the application toward the dense materials like superalloys or refractory alloys, the SPC method does not have such restrictions and thus this method can be utilized for a wider range of materials. It excels at identifying defects by detecting changes in the material's non-linearity, which can correlate to variations in the size, distribution, and type of porosity within the microstructure. When combined with advanced characterization techniques like laser doppler vibrometry (LDV) [69–71], contactless detection can be achieved thereby contributing to more flexibility to conduct structural health monitoring for more AM components with complex geometries, like lattice structures, for which transducers cannot be readily used due to size constraints.

It should be noted that the SPC method is not a 'ground-truth' technique and therefore the interpretation of the SPC-index requires comparison to a 'standard' pristine sample, or it must be initially guided by comparisons with other methods such as XCT. This guidance can then provide SPC the ability to directly quantify the exact changes in the size of pores and spatial distribution in samples, independent of their size, shape and geometry.

The next steps in ensuring the success of SPC as a rapid non-destructive inspection technique, involves guidance from acoustic wave propagation simulations that can examine the nonlinear acoustic response of materials as a function of different defect distributions. The combination of such simulation data in conjunction with targeted ground-truth characterization data (e.g. XCT), can accelerate the utilization of SPC for robust and reliable inspection of parts with the ability to detect changes in the acoustic response due to the presence of even solitary defects that are deleterious to the integrity of engineered parts.

On the other hand, XCT yields a more detailed and precise estimation of defect properties, including size, distribution, and morphologies. This explicit form of data is essential for validating and correlating the findings from SPC tests as it provides a direct visual representation of the internal features. When combined, the spatial data from XCT helps clarify changes in SPC values from different samples and hence strengthened the quantitative relationship between the microstructural characteristics and the acoustic response. Moreover, the microfocus XCT's high-resolution 3D imaging capabilities allow for the visualization of the porosity down to the micron-scale, and validates the ability of the SPC method to detect the presence of micron-sized defects in samples 1, 4, and 5.

Lastly, OM serves as an additional validation tool, offering surface-level visualization down to sub-micron scale that can be correlated with XCT data to confirm the accuracy of the visualized and reconstructed 3D structure. Although OM is limited to destructive analysis and may not capture the full distribution of porosity due to their inhomogeneous distribution, it remains a valuable and established technique for validating the results from XCT.

This study demonstrated the benefits of combining microfocus XCT and SPC for non-destructive evaluation, providing new insights into how non-linear acoustic waves are influenced by the size and spatial distribution of porosity in additively manufactured IN718 samples. This integration has the potential to transform SPC from a qualitative to a quantitative analysis method. Through the statistical analysis via XCT data, the size and distribution of porosity were determined to have a more profound impact on non-linear acoustic response in addition to the volume fraction. By incorporating the SPC results with the XCT data, we can correlate SPC values to the size, volume fraction, and spatial distribution of porosity. This will enable the SPC technique to non-destructively evaluate the defects within the AM components with different sizes and geometries and may serve as a substitute for the more costly and time consuming XCT. As illustrated in Fig. 14, developing a robust and validated database combined with machine learning approaches will enable further correlation between SPC and XCT. With a sufficient database, the SPC method would provide more rapid non-destructive evaluation to ensure the quality and reliability of additively manufactured products without the limitations of sample

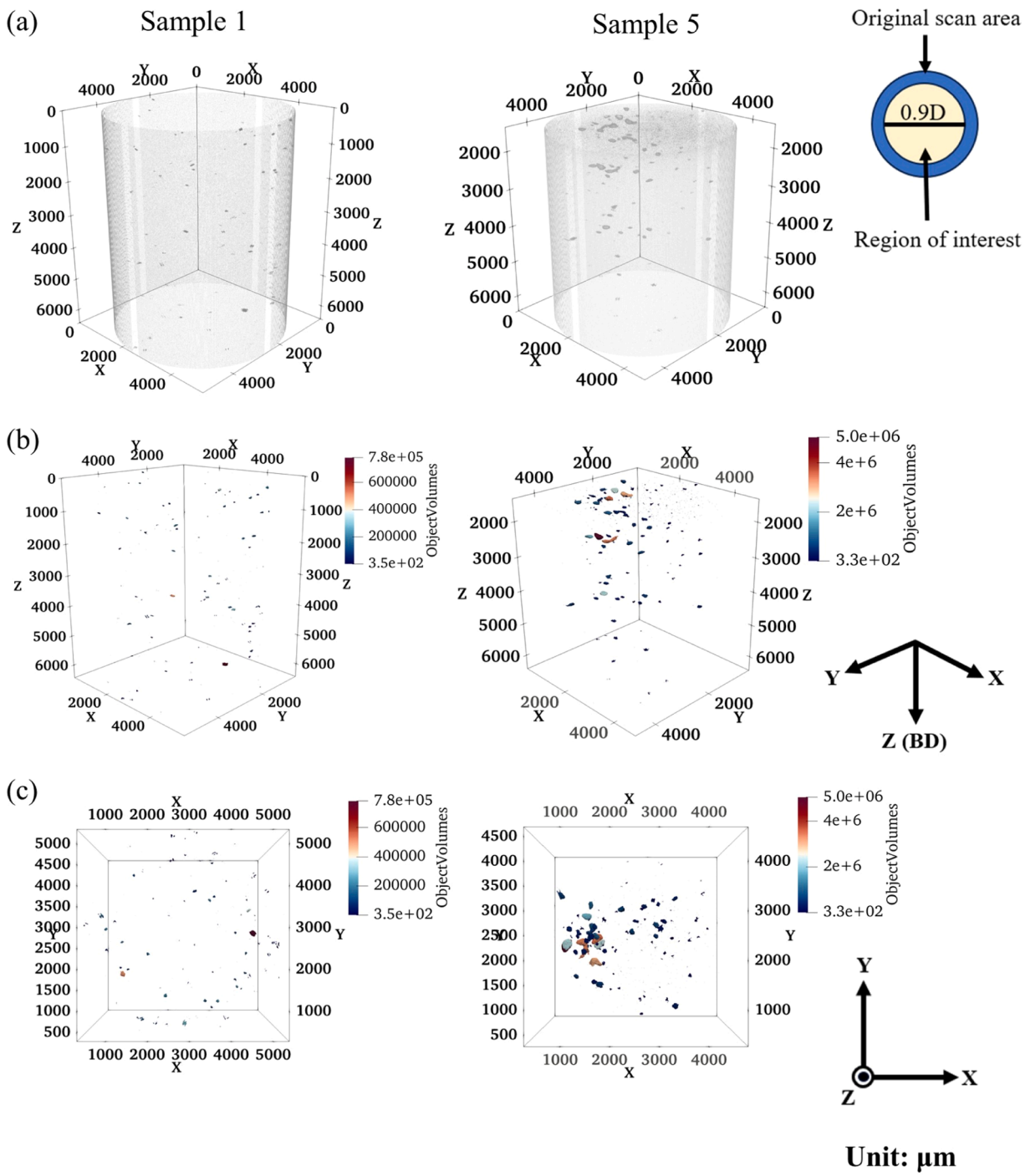

Fig. 13. 3D visualization of XCT data and surface extraction results focusing on a region of interest that is 90 % of the gauge diameter for samples 1 and 5: (a) XCT data visualization before binarization, (b) surface extraction results shown from an isometric view, and (c) surface extraction results shown from a top view. Note that the visualizations are extracted from the same data used in Fig. 8 for samples 1 and 5.

dimensions, geometries, and X-ray attenuation. Utilizing advanced acoustic detection methods like laser doppler vibrometry and acoustic wave propagation simulations, the integrated XCT and machine learning-driven SPC approach could be combined with in-situ process as well as evaluation of critical individual defects, potentially helping to accelerate the qualification and standardization of different components fabricated via additive manufacturing.

6. Conclusion

This study elucidates the influence of porosity characteristics on the non-linear acoustic response of IN718 fabricated via PBF-LB/M. By correlating the SPC method with microfocus XCT non-destructive techniques, we have generated new knowledge that now links physical attributes of porosities to the magnitudes of the SPC results. The critical findings are outlined as follows:

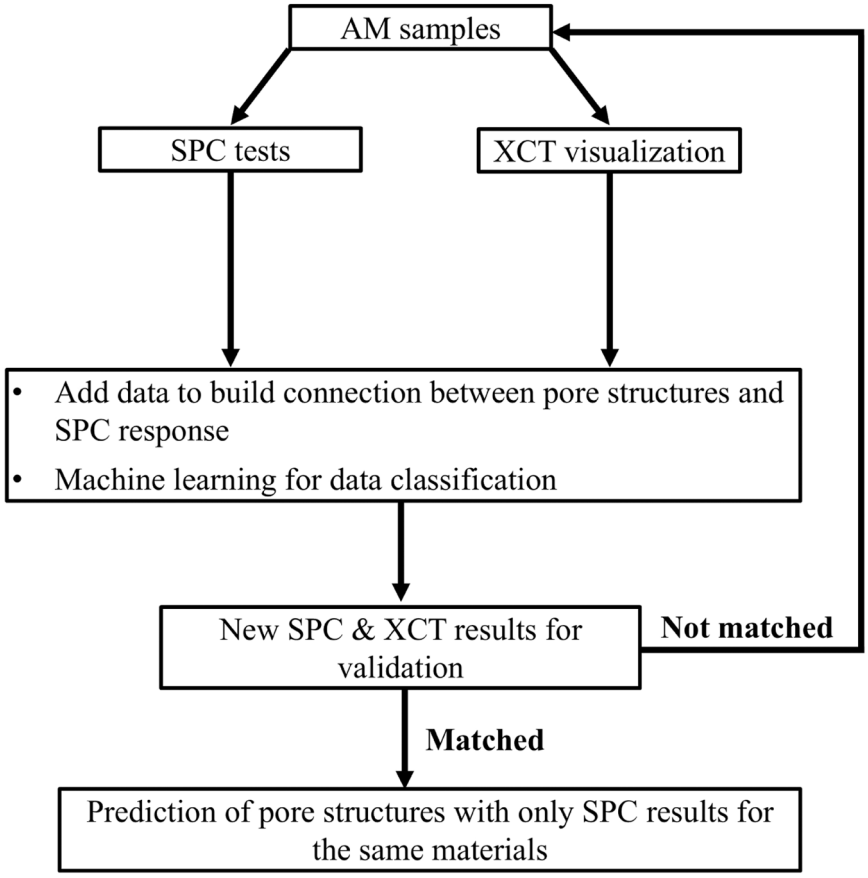

Fig. 14. Schematic illustration showing the workflow for applying SPC method to predict porosity structures in AM samples.

- The non-linear acoustical response, indicated by the number of peaks and SPC values, is predominantly affected by the porosity size distribution in addition to the volume fraction. Samples with large lack-of-fusion defects exhibited a less pronounced generation of side-bands, leading to a rapid decrease in peak counts as the threshold increased. This was evidenced by the lower average peak counts and SPC values observed in samples 2 and 3 in contrast to 1, 4, and 5 which displayed smaller and more uniformly distributed porosities.
- By examining the distances between closest 20 neighbors within samples containing the similar volume fraction of porosities, the increases in magnitudes of number of peak counts and SPC were found to be inversely proportional to the degree of clustering of porosities. The findings highlight the distribution of porosities could also significantly impact the non-linear acoustic response.
- The comparative study of SPC and XCT underlined the potential of utilizing both methods for a more comprehensive non-destructive evaluation of defects. SPC serves as an effective preliminary screening tool, while XCT offers a more detailed and precise estimation of defect properties in a selected area. Through data-driven analysis, this combination offers a novel and cost-effective solution, using ultrasonic and SPC methods, to rapidly understand the as-built properties during the AM process, regardless of the component's geometry.

CRediT authorship contribution statement

Michael Reale: Writing – review & editing, Resources, Project administration. **Tribikram Kundu:** Writing – review & editing, Methodology, Conceptualization. **Devin Bayly:** Writing – review & editing, Visualization, Methodology. **Brian Gockel:** Writing – review & editing, Resources, Project administration. **Krishna Muralidharan:** Writing – review & editing, Supervision, Project administration, Methodology, Funding acquisition, Conceptualization. **Sammy Tin:** Writing – review & editing, Supervision, Resources. **I-Ting Ho:** Writing – original draft, Visualization, Validation, Methodology, Investigation, Data curation, Conceptualization.

Declaration of Competing Interest

The authors declare that they have no known competing financial interests or personal relationships that could have appeared to influence the work reported in this paper.

Acknowledgement

This material is submitted with the understanding that right of reproduction for governmental purposed is reserved for the Office of Naval Research, Arlington, VA 22203–1995. Dr. I-Ting Ho also acknowledges the support from the National Science Foundation sponsored "New Frontiers of Sound Science and Technology Center" at the University of Arizona (Grant No. 2242925).

Data Availability

No data was used for the research described in the article.

References

[1] E.D.B.C. Hautfenne, S. Nardone, Influence of Heat Treatments And Build Orientation On The Creep Strength Of Additive Manufactured IN718, in: 4th Int. ECCC Conf., Dusseldorf, Germany, n.d.
[2] B. Shassere, D. Greeley, A. Okello, M. Kirka, P. Nandwana, R. Dehoff, Correlation of microstructure to creep response of hot isostatically pressed and aged electron

beam melted Inconel 718, Metall. Mater. Trans. A 49 (2018) 5107–5117, https://doi.org/10.1007/s11661-018-4812-z.
[3] A. Strondl, M. Palm, J. Gnauk, G. Frommeyer, Microstructure and mechanical properties of nickel based superalloy IN718 produced by rapid prototyping with electron beam melting (EBM), Mater. Sci. Technol. 27 (2011) 876–883, https://doi.org/10.1179/026708309X12468927349451.
[4] E.A. Lass, M.R. Stoudt, M.E. Williams, M.B. Katz, L.E. Levine, T.Q. Phan, T. H. Gnaeupel-Herold, D.S. Ng, Formation of the Ni3Nb δ-phase in stress-relieved Inconel 625 produced via laser powder-bed fusion additive manufacturing, Metall. Mater. Trans. A Phys. Metall. Mater. Sci. 48 (2017), https://doi.org/10.1007/s11661-017-4304-6.
[5] H. Hilal, R. Lancaster, S. Jeffs, J. Boswell, D. Stapleton, G. Baxter, The influence of process parameters and build orientation on the creep behaviour of a laser powder bed fused Ni-based superalloy for aerospace applications, Materials 12 (2019) 1390, https://doi.org/10.3390/ma12091390.
[6] S.J. Davies, S.P. Jeffs, M.P. Coleman, R.J. Lancaster, Effects of heat treatment on microstructure and creep properties of a laser powder bed fused nickel superalloy, Mater. Des. 159 (2018) 39–46, https://doi.org/10.1016/j.matdes.2018.08.039.
[7] S.J. Håkan Brodin, Olov Andersson, Mechanical Testing of A Selective Laser Melted Superalloy, in: 13th Int. Conf. Fract., Beijing, China, 2013.
[8] M.J..Donachie, Superalloys: A Technical Guide, 2nd Edition, America (NY). (2002). https://doi.org/10.1361.
[9] X. Wang, N. Read, L.N. Carter, R.M. Ward, M.M. Attallah, Defect formation and its mitigation in selective laser melting of high γ′ Ni-base superalloys, Proc. Int. Symp. Superalloys. 2016-Janua (2016) 351–358, https://doi.org/10.1002/9781119075646.ch38.
[10] Y.T. Tang, C. Panwisawas, J.N. Ghoussoub, Y. Gong, J.W.G. Clark, A.A.N. Németh, D.G. McCartney, R.C. Reed, Alloys-by-design: application to new superalloys for additive manufacturing, Acta Mater. 202 (2021) 417–436, https://doi.org/10.1016/j.actamat.2020.09.023.
[11] R. Engeli, T. Etter, S. Hövel, K. Wegener, Processability of different IN738LC powder batches by selective laser melting, J. Mater. Process. Technol. 229 (2016) 484–491, https://doi.org/10.1016/j.jmatprotec.2015.09.046.
[12] I..Lopez-Galilea, B..Ruttert, W..Theisen, Integrated HIP-Heat Treatment of Ni-Base Superalloys Fabricated by SLM, in: Euro PM 2018 Congr. Exhib., European Powder Metallurgy Association (EPMA), 2020.
[13] Y.C.Hagedorn, J.Risse, W.Meiners, N.Pirch, K.Wissenbach, R.Poprawe, Processing of Nickel Based Superalloy MAR M-247 by Means of High Temperature - Selective Laser Melting (HT - SLM), in: High Value Manuf. Adv. Res. Virtual Rapid Prototyp. - Proc. 6th Int. Conf. Adv. Res. Rapid Prototyping, VR@P 2013, 2014. ⟨https://doi.org/10.1201/b15961-54⟩.
[14] J. Yang, F. Li, Z. Wang, X. Zeng, Cracking behavior and control of Rene 104 superalloy produced by direct laser fabrication, J. Mater. Process. Technol. 225 (2015), https://doi.org/10.1016/j.jmatprotec.2015.06.002.
[15] L.E. Murr, E. Martinez, X.M. Pan, S.M. Gaytan, J.A. Castro, C.A. Terrazas, F. Medina, R.B. Wicker, D.H. Abbott, Microstructures of Rene 142 nickel-based superalloy fabricated by electron beam melting, Acta Mater. 61 (2013), https://doi.org/10.1016/j.actamat.2013.04.002.
[16] A. Mostafaei, R. Ghiaasiaan, I.-T. Ho, S. Strayer, K.-C. Chang, N. Shamsaei, S. Shao, S. Paul, A.-C. Yeh, S. Tin, A.C. To, Additive Manufacturing of Nickel-based superalloys: a state-of-the-art review on process-structure-defect-property relationship, Prog. Mater. Sci. (2023), https://doi.org/10.1016/j.pmatsci.2023.101108.
[17] T. Huynh, A. Mehta, K. Graydon, J. Woo, S. Park, H. Hyer, L. Zhou, D.D. Imholte, N.E. Woolstenhulme, D.M. Wachs, Y. Sohn, Microstructural development in Inconel 718 Nickel-based superalloy additively manufactured by laser powder bed fusion, Metallogr. Microstruct. Anal. 11 (2022), https://doi.org/10.1007/s13632-021-00811-0.
[18] M. Tang, P.C. Pistorius, J.L. Beuth, Prediction of lack-of-fusion porosity for powder bed fusion, Addit. Manuf. 14 (2017) 39–48, https://doi.org/10.1016/j.addma.2016.12.001.
[19] A. DuPlessis, S.G. LeRoux, J. Els, G. Booysen, D.C. Blaine, Application of microCT to the non-destructive testing of an additive manufactured titanium component, Case Stud. Nondestruct. Test. Eval. 4 (2015), https://doi.org/10.1016/j.csndt.2015.09.001.
[20] M.L. Wang, X.G. Yang, B. Li, D.Q. Shi, G.L. Miao, S.Q. Guo, Y.S. Fan, The dominant role of defects on fatigue behaviour of a SLM Ni-based superalloy at elevated temperature, Int. J. Fatigue 176 (2023), https://doi.org/10.1016/j.ijfatigue.2023.107894.
[21] M.S. Dodaran, M. Muhammad, N. Shamsaei, S. Shao, Synergistic effect of microstructure and defects on the initiation of fatigue cracks in additively manufactured Inconel 718, Int. J. Fatigue 162 (2022), https://doi.org/10.1016/j.ijfatigue.2022.107002.
[22] E. Sadeghi, G. Asala, P. Karimi, D. Deng, J. Moverare, T. Hansson, Fatigue crack initiation and propagation in Alloy 718 with a bimodal grain morphology built via electron beam-powder bed fusion, Mater. Sci. Eng. A 827 (2021), https://doi.org/10.1016/j.msea.2021.142051.
[23] J.L. McNeil, K. Sisco, C. Frederick, M. Massey, K. Carver, F. List, C. Qiu, M. Mader, S. Sundarraj, S.S. Babu, In-situ monitoring for defect identification in Nickel alloy complex geometries fabricated by L-PBF additive manufacturing, Metall. Mater. Trans. A Phys. Metall. Mater. Sci. 51 (2020), https://doi.org/10.1007/s11661-020-06036-0.
[24] F.H. Kim, H. Yeung, E.J. Garboczi, Characterizing the effects of laser control in laser powder bed fusion on near-surface pore formation via combined analysis of in-situ melt pool monitoring and X-ray computed tomography☆, Addit. Manuf. 48 (2021) https://doi.org/10.1016/j.addma.2021.102372.
[25] Z. Snow, B. Diehl, E.W. Reutzel, A. Nassar, Toward in-situ flaw detection in laser powder bed fusion additive manufacturing through layerwise imagery and machine learning, J. Manuf. Syst. 59 (2021), https://doi.org/10.1016/j.jmsy.2021.01.008.
[26] S. Sampath, R. Dhayalan, A. Kumar, N.N. Kishore, H. Sohn, Evaluation of material degradation using phased array ultrasonic technique with full matrix capture, Eng. Fail. Anal. 120 (2021), https://doi.org/10.1016/j.engfailanal.2020.105118.
[27] C. Bermes, J.Y. Kim, J. Qu, L.J. Jacobs, Nonlinear Lamb waves for the detection of material nonlinearity, Mech. Syst. Signal Process. 22 (2008), https://doi.org/10.1016/j.ymssp.2007.09.006.
[28] M. Amura, M. Meo, F. Amerini, Baseline-free estimation of residual fatigue life using a third order acoustic nonlinear parameter, J. Acoust. Soc. Am. 130 (2011), https://doi.org/10.1121/1.3621714.
[29] L. Qiu, S. Yuan, Q. Bao, H. Mei, Y. Ren, Crack propagation monitoring in a full-scale aircraft fatigue test based on guided wave-Gaussian mixture model, Smart Mater. Struct. 25 (2016), https://doi.org/10.1088/0964-1726/25/5/055048.
[30] S. Sampath, H. Sohn, Detection and localization of fatigue crack using nonlinear ultrasonic three-wave mixing technique, Int. J. Fatigue 155 (2022), https://doi.org/10.1016/j.ijfatigue.2021.106582.
[31] S.Sampath, H.Sohn, Detection of Material Nonlinearity Using Nonlinear Ultrasonic Three-wave Mixing Technique, in: 2021. ⟨https://doi.org/10.1117/12.2581415⟩.
[32] N.A. Chrysochoidis, T.T. Assimakopoulou, D.A. Saravanos, Nonlinear wave structural health monitoring method using an active nonlinear piezoceramic sensor for matrix cracking detection in composites, J. Intell. Mater. Syst. Struct. 26 (2015), https://doi.org/10.1177/1045389X14549865.
[33] J. Segers, S. Hedayatrasa, G. Poelman, W. VanPaepegem, M. Kersemans, Broadband nonlinear elastic wave modulation spectroscopy for damage detection in composites, Struct. Heal. Monit. 21 (2022), https://doi.org/10.1177/14759217211002562.
[34] P. Liu, H. Sohn, S. Yang, H.J. Lim, Baseline-free fatigue crack detection based on spectral correlation and nonlinear wave modulation, Smart Mater. Struct. 25 (2016), https://doi.org/10.1088/0964-1726/25/12/125034.
[35] S. Gwon, E. Ahn, M. Shin, J.Y. Kim, G. Kim, Assessment of internal curing of cellulose microfibers-incorporated cement composites using destructive and nondestructive methods, Constr. Build. Mater. 352 (2022), https://doi.org/10.1016/j.conbuildmat.2022.129004.
[36] J. Jin, M.G. Moreno, J. Riviere, P. Shokouhi, Impact-based nonlinear acoustic testing for characterizing distributed damage in concrete, J. Nondestruct. Eval. 36 (2017), https://doi.org/10.1007/s10921-017-0428-2.
[37] J.N. Eiras, T. Kundu, M. Bonilla, J. Payá, Nondestructive monitoring of ageing of alkali resistant glass fiber reinforced cement (GRC), J. Nondestruct. Eval. 32 (2013), https://doi.org/10.1007/s10921-013-0183-y.
[38] T.Kundu, Nonlinear Ultrasonic and Vibro-acoustical Techniques for Nondestructive Evaluation, 2018. ⟨https://doi.org/10.1007/978-3-319-94476-0⟩.
[39] H. Alnuaimi, U. Amjad, P. Russo, V. Lopresto, T. Kundu, Monitoring damage in composite plates from crack initiation to macro-crack propagation combining linear and nonlinear ultrasonic techniques, Struct. Heal. Monit. 20 (2021), https://doi.org/10.1177/1475921720922922.
[40] P. Liu, H. Sohn, Damage detection using sideband peak count in spectral correlation domain, J. Sound Vib. 411 (2017), https://doi.org/10.1016/j.jsv.2017.08.049.
[41] P. Liu, H. Sohn, T. Kundu, Fatigue crack localization using Laser nonlinear wave modulation spectroscopy (LNWMS), J. Korean Soc. Nondestruct. Test. 34 (2014), https://doi.org/10.7779/jksnt.2014.34.6.419.
[42] H. Alnuaimi, U. Amjad, S. Park, P. Russo, V. Lopresto, T. Kundu, An improved nonlinear ultrasonic technique for detecting and monitoring impact induced damage in composite plates, Ultrasonics 119 (2022), https://doi.org/10.1016/j.ultras.2021.106620.
[43] P. Liu, H. Sohn, T. Kundu, S. Yang, Noncontact detection of fatigue cracks by laser nonlinear wave modulation spectroscopy (LNWMS), NDT&E Int. 66 (2014), https://doi.org/10.1016/j.ndteint.2014.06.002.
[44] S. Basu, A. Thirumalaiselvi, S. Sasmal, T. Kundu, Nonlinear ultrasonics-based technique for monitoring damage progression in reinforced concrete structures, Ultrasonics 115 (2021), https://doi.org/10.1016/j.ultras.2021.106472.
[45] A. Castellano, A. Fraddosio, M.D. Piccioni, T. Kundu, Linear and nonlinear ultrasonic techniques for monitoring stress-induced damages in concrete, J. Nondestruct. Eval. Diagn. Progn. Eng. Syst. 4 (2021), https://doi.org/10.1115/1.4050354.
[46] S.H. Park, T. Kundu, A modified sideband peak count based nonlinear ultrasonic technique for material characterization, Ultrasonics 128 (2023), https://doi.org/10.1016/j.ultras.2022.106858.
[47] J. Ahrens, B. Geveci, C. Law, ParaView: an end-user tool for large-data visualization, Vis. Handb. (2005), https://doi.org/10.1016/B978-012387582-2/50038-1.
[48] C. Portaneri, M. Rouxel-Labbé, M. Hemmer, D. Cohen-Steiner, P. Alliez, Alpha wrapping with an offset, ACM Trans. Graph. 41 (2022), https://doi.org/10.1145/3528223.3530152.
[49] E. Fogel, M. Teillaud, The Computational Geometry Algorithms Library CGAL, ACM Commun. Comput. Algebr 49 (2015), https://doi.org/10.1145/2768577.2768579.
[50] T.K.F..Da, S..Loriot, M..Yvinec, 3D Alpha Shapes, CGAL User Ref. Man. 5.6.1 edit (2024).
[51] A. Zollanvari, Mach. Learn. Python (2023). ⟨https://doi.org/10.1007/978-3-031-33342-2⟩.
[52] P.Sarang, Thinking Data Science A Data Science Practitioner's Guide The Springer Series in Applied Machine Learning, 2023.

[53] H. Wadell, Volume, shape, and roundness of quartz particles, J. Geol. 43 (1935), https://doi.org/10.1086/624298.
[54] J. Elambasseril, S.L. Lu, Y.P. Ning, N. Liu, J. Wang, M. Brandt, H.P. Tang, M. Qian, 3D characterization of defects in deep-powder-bed manufactured Ti–6Al–4V and their influence on tensile properties, Mater. Sci. Eng. A 761 (2019), https://doi.org/10.1016/j.msea.2019.138031.
[55] J. Ye, A. Poudel, J. (Peter)Liu, A. Vinel, D. Silva, S. Shao, N. Shamsaei, Machine learning augmented X-ray computed tomography features for volumetric defect classification in laser beam powder bed fusion, Int. J. Adv. Manuf. Technol. 126 (2023), https://doi.org/10.1007/s00170-023-11281-9.
[56] R. Snell, S. Tammas-Williams, L. Chechik, A. Lyle, E. Hernández-Nava, C. Boig, G. Panoutsos, I. Todd, Methods for rapid pore classification in metal additive manufacturing, JOM 72 (2020), https://doi.org/10.1007/s11837-019-03761-9.
[57] H. Gong, K. Rafi, H. Gu, T. Starr, B. Stucker, Analysis of defect generation in Ti-6Al-4V parts made using powder bed fusion additive manufacturing processes, Addit. Manuf. 1 (2014), https://doi.org/10.1016/j.addma.2014.08.002.
[58] C. Pecorari, I. Solodov, Nonclassical nonlinear dynamics of solid surfaces in partial contact for NDE Applications, Univers. Nonclassical Nonlin. (2006), https://doi.org/10.1007/978-0-387-35851-2_19.
[59] M.H. Hafezi, R. Alebrahim, T. Kundu, Peri-ultrasound for modeling linear and nonlinear ultrasonic response, Ultrasonics 80 (2017), https://doi.org/10.1016/j.ultras.2017.04.015.
[60] R.F, T.K.S.H. Park, I. Bokhari, H. Alnuaimi, U. Amjad, Early detection of steel tube welded joint failure using SPC-I nonlinear ultrasonic technique, Struct. Heal. Monit. Int. J. in press (2024).
[61] S.Park, I.Bokhari, H.Alnuaimi, U.Amjad, R.Fleischman, T.Kundu, Inspection Of Steel Tube Welded Joint Using Nonlinear Ultrasonic Technique, in: 2022. ⟨https://doi.org/10.1117/12.2611920⟩.
[62] T. Arumaikani, S. Sasmal, T. Kundu, Detection of initiation of corrosion induced damage in concrete structures using nonlinear ultrasonic techniques, J. Acoust. Soc. Am. 151 (2022), https://doi.org/10.1121/10.0009621.
[63] S.H. Park, H. Alnuaimi, A. Hayes, M. Sitkiewicz, U. Amjad, K. Muralidharan, T. Kundu, Nonlinear acoustic technique for monitoring porosity in additively manufactured parts, J. Nondestruct. Eval. Diagn. Progn. Eng. Syst. 5 (2022), https://doi.org/10.1115/1.4053252.
[64] G. Zhang, X. Li, S. Zhang, T. Kundu, Sideband peak count-index technique for monitoring multiple cracks in plate structures using ordinary state-based peri-ultrasound theory, J. Acoust. Soc. Am. 152 (2022), https://doi.org/10.1121/10.0015242.
[65] G. Zhang, X. Li, T. Kundu, Ordinary state-based peri-ultrasound modeling to study the effects of multiple cracks on the nonlinear response of plate structures, Ultrasonics 133 (2023), https://doi.org/10.1016/j.ultras.2023.107028.
[66] G. Zhang, X. Li, T. Li, T. Kundu, Ordinary state-based peri-ultrasound modeling for monitoring crack propagation in plate structures using sideband peak count-index technique, J. Sound Vib. 568 (2024), https://doi.org/10.1016/j.jsv.2023.117962.
[67] Y. Zheng, R.G. Maev, I.Y. Solodov, Nonlinear acoustic applications for material characterization: a review, Can. J. Phys. 77 (1999), https://doi.org/10.1139/cjp-77-12-927.
[68] Y. Li, S. Hu, C.H. Henager, Microstructure-based model of nonlinear ultrasonic response in materials with distributed defects, J. Appl. Phys. 125 (2019), https://doi.org/10.1063/1.5083957.
[69] S.J. Rothberg, M.S. Allen, P. Castellini, D. DiMaio, J.J.J. Dirckx, D.J. Ewins, B. J. Halkon, P. Muyshondt, N. Paone, T. Ryan, H. Steger, E.P. Tomasini, S. Vanlanduit, J.F. Vignola, An international review of laser Doppler vibrometry: Making light work of vibration measurement, Opt. Lasers Eng. 99 (2017), https://doi.org/10.1016/j.optlaseng.2016.10.023.
[70] E.P. Tomasini, P. Castellini, Laser Doppler Vibrometry, Springer Berlin Heidelberg, 2020, https://doi.org/10.1142/9789812834133_0010.
[71] P. Liu, L. Yang, K. Yi, T. Kundu, H. Sohn, Application of Nonlinear Ultrasonic Analysis for in Situ Monitoring of Metal Additive Manufacturing, Struct. Heal. Monit. 22 (2023), https://doi.org/10.1177/14759217221113447.